

Article

Effect of Thermodenuding on the Structure of Nascent Flame Soot Aggregates

Janarjan Bhandari ^{1,*}, Swarup China ^{1,†}, Timothy Onasch ^{2,3}, Lindsay Wolff ³, Andrew Lambe ^{2,3}, Paul Davidovits ³, Eben Cross ², Adam Ahern ⁴, Jason Olfert ⁵, Manvendra Dubey ⁶ and Claudio Mazzoleni ^{1,*}

¹ Department of Physics and Atmospheric Sciences Program, Michigan Technological University, Houghton, MI 49931, USA; schina@mtu.edu

² Aerodyne Research Inc., Billerica, MA 01821, USA; onasch@aerodyne.com (T.O.); lambe@aerodyne.com (A.L.); escross@aerodyne.com (E.C.)

³ Chemistry Department, Boston College, Chestnut Hill, MA 02467, USA; lrwolff@aerodyne.com (L.W.); davidovi@bc.edu (P.D.)

⁴ Centre for Atmospheric Particle Studies, Carnegie Mellon University, Pittsburgh, PA 15232, USA; aahern@andrew.cmu.edu

⁵ Department of Mechanical Engineering, University of Alberta, Edmonton, AB T6G 2G8, Canada; jolfert@ualberta.ca

⁶ Earth and Environmental Sciences Division, Los Alamos National Laboratory, Los Alamos, NM 87545, USA; dubey@lanl.gov

* Correspondence: jbandar@mtu.edu (J.B.); cmazzoleni@mtu.edu (C.M.)

† Current address: Pacific Northwest National Laboratory, Richland, WA 99354, USA.

Received: 27 July 2017; Accepted: 31 August 2017; Published: 6 September 2017

Abstract: The optical properties (absorption and scattering) of soot particles depend on soot size and index of refraction, but also on the soot complex morphology and the internal mixing with materials that can condense on a freshly emitted (nascent) soot particle and coat it. This coating can affect the soot optical properties by refracting light, or by changing the soot aggregate structure. A common approach to studying the effect of coating on soot optical properties is to measure the absorption and scattering coefficients in ambient air, and then measure them again after removing the coating using a thermodenuder. In this approach, it is assumed that: (1) most of the coating material is removed; (2) charred organic coating does not add to the refractory carbon; (3) oxidation of soot is negligible; and, (4) the structure of the pre-existing soot core is left unaltered, despite the potential oxidation of the core at elevated temperatures. In this study, we investigated the validity of the last assumption, by studying the effect of thermodenuding on the morphology of nascent soot. To this end, we analyzed the morphological properties of laboratory generated nascent soot, before and after thermodenuding. Our investigation shows that there is only minor restructuring of nascent soot by thermodenuding.

Keywords: thermodenuding; soot morphology; aggregates; compaction; restructuring

1. Introduction

Soot particles are mostly composed of refractory carbonaceous material that forms from incomplete combustion during burning activities [1]. A nascent soot particle appears as a fractal-like (sometimes referred to as a lacy) aggregate of small spherules (called nanospheres or monomers) [2] and its structure is scale invariant [3]. Here, the term “nascent” is used to refer to freshly emitted soot particles that have a negligible coating on the monomers. The diameter of these monomers varies in a range from 10 nm to more than 50 nm, depending on the fuel source and combustion conditions [4–7]. During the atmospheric processing, soot particles interact with organic and inorganic materials (in the form of aerosol or condensable vapors). During these interactions, soot undergoes

morphological changes including compaction, coagulation, and coating [8]. Combustion generated nascent soot aggregates often have different kinds of polycyclic aromatic hydrocarbons (PAHs) that thinly coat the monomers, depending upon the flaming conditions and fuel types, even in very controlled combustions [9]. In this case, coating is acquired at the source, and not added later through atmospheric processing. The degree of coating in atmospheric particles is very variable [6,8,10–14]. In some studies, thinly coated soot particles have been found in large fractions in the atmosphere. For example, in the study by China et al. [6], a large fraction (by number) of freshly emitted soot particles collected on freeway on ramps were thinly coated (72%). In another field study, carried out at Pico Mountain Observatory in the Azores, China et al. [8] found that 37% of the soot particles in one sample, were thinly coated, even after days of atmospheric processing during the long range transport in the free troposphere from the source. These two studies were carried out at very different locations (very near the source in the first study, and very far from the source in the second study), showing that thinly coated soot particles can exist in the atmosphere in different environments and geographic locations. In another study, in two plumes one sampled from Mexico City and one from outside of Mexico City, Adachi and Buseck [4] found that 7% of particles were soot without coating. Coating or internal mixing in general, changes the optical properties of soot, even when the structure of the refractory components remains the same. These changes consequently affect the radiative forcing of soot [15–22]. Several studies have also shown that coating of soot by partially-absorbing or non-absorbing materials increases the absorption and scattering cross sections [13,18,23–25]. These increases are termed “absorption and scattering enhancements” (E_{abs} and E_{sca}). The enhancement is typically calculated as the ratio of the light absorption or scattering coefficient of the coated soot to the light absorption or scattering coefficient of the soot core, after the coating material has been removed [18].

Thermodenuders (TDs) that remove the coating by evaporation, are often used in the field and in the laboratory to study and quantify these optical enhancements [16,26–28]. During the thermodenuding process, coated soot particles are passed through a heated column, typically at ~200–300 °C to evaporate the volatile coating material while leaving behind the refractory soot [29,30]. The temperature gradient within the TD can result in particle losses due to thermophoretic forces, though these losses can be measured and accounted for [29]. To correctly assess the E_{abs} and E_{sca} using a TD, one needs to make the following assumptions: (1) most of the coating material is removed from the soot by the TD; (2) organic coating material does not transform into refractory carbon due to charring; (3) refractory carbon is not oxidized to a substantial extent under elevated temperatures; and, (4) the structure of the refractory soot particle is unaffected, meaning that the thermodenuding process alone does not induce restructuring of the core lacy soot aggregates.

Contrary to assumption (1), thermodenuding may not remove refractory particulate material, such as some inorganic salts, and may not remove all of the non-refractory material from soot particles [23]. For example, Liu et al. [13] observed that denuded soot still contained heavily coated soot particles, although, in a smaller fraction with respect to ambient particles, suggesting that the TD may not completely remove the coating. Healy et al. [12] found that, on average, only 74% of the mass of coating material was removed from soot samples after thermodenuding. The mass removal efficiency by the TD was even less (approximately 60%) for wildfire emission samples. Swanson and Kittelson [31] have also cautioned about semi-volatile particle artifacts due to incomplete removal of evaporated compounds in the TD. Similarly, Knox et al. [32] found that there was no significant difference in the mass absorption cross section between thermodenuded and non-thermodenuded aged-soot particles as compared to fresh soot, due to the incomplete removal of coating materials from aged soot particles. On the other hand, Khalizov et al. [33] hypothesized that the thermodenuder may remove all of the coating material from ambient soot, including the coating acquired during atmospheric processing, as well as the nascent coating present on soot at the source, and therefore, they suggested that the denuded particles cannot represent the nascent soot morphology.

Next, we briefly review assumptions (2) and (3). The elevated temperatures during the thermodenuding process may cause charring of some organic matter into refractory, elemental

carbon, and/or some oxidation of the carbonaceous matter. The charring of organic particulate material into elemental carbon is a known phenomenon under the elevated temperatures employed in organic carbon and elemental carbon (OCEC) analyses [34,35]. Issues that influence the charring include temperatures and residence times, as well as chemical composition. Charring is likely to be more of an issue for oxidized organics, such as biomass burning or secondary organic aerosol (SOA), than reduced organics, such as efficient combustion products (i.e., diesel and laboratory flame soot) [36,37]. Two significant differences between OCEC and thermodenuding include: (1) OCEC techniques typically operate at higher temperatures than TDs, and (2) OCEC charring occurs in a helium atmosphere, whereas thermodenuding occurs in air (i.e., oxidizing environment). Thus, at a low temperature (<300 °C), thermodenuding will be less likely to char, and the particles may be more susceptible to oxidation due to an oxidizing environment. Oxidation of refractory carbon soot typically occurs at significantly elevated temperatures, but can occur at lower temperatures as well, especially if catalyzed by impurities in the soot [38]. Soot oxidation is likely limited in thermodenuding due to the low temperatures and the relatively short residence time, but this issue will require more study in the future.

We finally discuss the assumption (4), which is the focus of our study. Previous studies have shown that nascent soot particles can restructure during the condensation or evaporation of the coating material, depending on their surface tension [39–41]. Xue et al. [28] found significant restructuring of soot particles when the particles were first coated with glutaric acid and then denuded. Ghazi and Olfert [16] reported the dependence of soot restructuring on the mass amount of different coating material types. This restructure alone can affect the optical properties of soot particles. For example, a laboratory study was performed on soot compacted upon humidification; the study measured modest changes in the absorption cross-section (5% to 14%), but the extinction cross-section was much more sensitive to compaction, with changes of more than 30% [42]. Similarly, China et al. [8,43], using numerical simulations, predicted small changes in the absorption cross-section (a few percent), but a much more substantial change in the total scattering cross section (up to ~300%) upon soot compaction. In addition to affecting the optical properties, changes in the soot structure can also affect the results of laser induced incandescence measurements [5]. Finally, the condensation of secondary organic matter preferentially takes place in empty pores on soot particles, and therefore, it is possible that compaction will affect secondary organic condensation on soot [44]. Two potential explanations for the coated soot restructuring detected during these studies can be: (1) Soot might be compacted during condensation of the coating materials due to surface tension effects [14,41,45,46]. (2) The removal of the coating material during the subsequent thermodenuding may cause compaction when the coating evaporates, still due to surface tension effects [39,40]. However, we hypothesize a third potential pathway, in which soot restructuring might take place solely due to the thermodenuding process, through the added thermal energy. Coating alone might not cause full compaction (i.e., completely collapsed structure). For example, in an experiment, Leung et al. [47] found that the coating did not restructure the soot aggregate even when the aggregate was completely covered by the coating material. Some coating material indeed results in substantial or even maximum compaction, but other coating materials actually result in negligible compaction. A clear example is shown in a laboratory study where particles coated with sulfuric acid did undergo severe restructuring, while the soot particles coated by dioctyl sebacate showed only minimal or no compaction [9]. Also, from Mexico City samples, Adachi and Buseck [4] found coated soot but with lacy structure. For the case of coated but yet only partially compacted soot, thermodenuding may facilitate further restructuring. The coating material can become less viscous at the elevated temperatures during the thermodenuding and restructure the soot core [47].

Next, we will discuss some lines of evidence that the thermodenuding process alone can in some cases, favor the compaction of lacy aggregates of various materials, even in the absence of coating material that condenses onto the primary aggregates. If a similar process happens for ambient soot, such a process would potentially bias the measured properties (e.g., absorption or scattering

enhancements) of soot when a thermodenuder is used. The main objective of our study is to test this hypothesis, to assure that the thermodenuding process alone does not introduce this bias. A couple of potential restructuring processes induced during thermodenuding, are discussed next:

- (a) When heated, fractal-like aggregates of metal nanoparticles, such as silver, copper, and metallic oxides (e.g., titania), have been found to restructure to more compact morphologies at temperatures well below the bulk material melting points. For example, thermal restructuring has been found in silver aggregates, even at temperatures as low as 100 °C, with full compaction at just 350 °C (much below the melting temperature of silver), while the primary particle size remained unchanged [48,49]. Another study found that aggregates of titania started to collapse when temperatures reached 700 °C [50]. These authors speculated that the heating causes the weakest branches in an aggregate to rotate around their contact points, resulting in the aggregate restructuring. Alternatively, Schmidt-Ott [51] hypothesized that the monomers in silver nanoparticles aggregates might slide on each other when heated, also causing compaction. Both processes would restructure the aggregates without a complete breakage of the bonds between the monomers due to Van der Waals forces.
- (b) As mentioned earlier, nascent soot aggregates typically have polycyclic aromatic hydrocarbons thinly coating them. This nascent coating could play a role in determining the soot structure if the coating properties (i.e., viscosity and surface tension) change at the higher temperature of the thermodenuder. Chen et al. [52] found that some polycyclic aromatic hydrocarbons, like phenanthrene and flouranthene, when present as a subnanometer layer on soot, behaved as subcooled liquid that weakened the bonds between the monomers, allowing them to slide and roll over each other and resulting in soot restructuring. Rothenbacher et al. [53] provided evidence that thermodenuding might make a difference in the strength of the adhesive bonds between the monomers. For aged soot, they found a higher degree of fragmentation for thermodenuded particles (75% at 280 °C) than for untreated (not thermodenuded) particles (60%) when impacted at ~200 m/s. The degree of fragmentation was defined as the fraction of broken bonds in an aggregate. Although the process involved both the effect of coating and impaction, the higher degree of fragmentation for thermodenuded particles suggests that the thermal energy has a role on the increased degree of fragmentation.

These lines of evidence motivated us to study the potential effects of thermodenuding on the specific case of nascent soot. With this goal in mind, we analyzed the structure of laboratory generated nascent soot particles produced from two different fuel sources (ethylene flame and methane flame) and size selected at different mobility diameters before and after thermodenuding. This assessment is important for evaluating the potential biases that might be introduced by thermodenuding while, for example, estimating the absorption or scattering enhancements of laboratory or ambient soot particles.

2. Experiments

2.1. Experimental Setup and Sample Collection

We analyzed five pairs of mobility-selected soot samples collected during two different experiments: the Boston College Experiment 2 (BC2) and the Boston College Experiment 4 (BC4). The sampling schematics are shown in the Figure 1a,b. None of the soot particles were coated with additional external coating material, and the minimal coating present on the nascent soot was solely due to the fuel residuals accumulated during the combustion and dilution processes.

Three soot sample sets were collected during BC2 from the combustion of ethylene and oxygen using a premixed flat flame burner [9]. The fuel equivalence ratio (ϕ) for all the three sample sets was 2.1. A TD [29] was used to remove volatile components from the nascent soot particles. The heating section of the TD was set at 250 °C to vaporize the non-refractory soot components, which were absorbed by a charcoal section maintained at room temperature. Particles for a range of mobility

diameters (d_m) were selected to investigate the effect of thermodenuding on particle size. For our investigation, we selected three sets of nascent vs. nascent-denuded soot particles with $d_m = 153$ nm, 181 nm and 250 nm for nascent and $d_m = 151$ nm, 175 nm, and 241 nm for the corresponding denuded soot particles. Soot particles were collected on 13 mm diameter Nuclepore polycarbonate filters having a pore size of $0.3 \mu\text{m}$ (Whatman Inc., Chicago, IL, USA). Additional details regarding the BC2 experimental set-up are provided elsewhere [9].

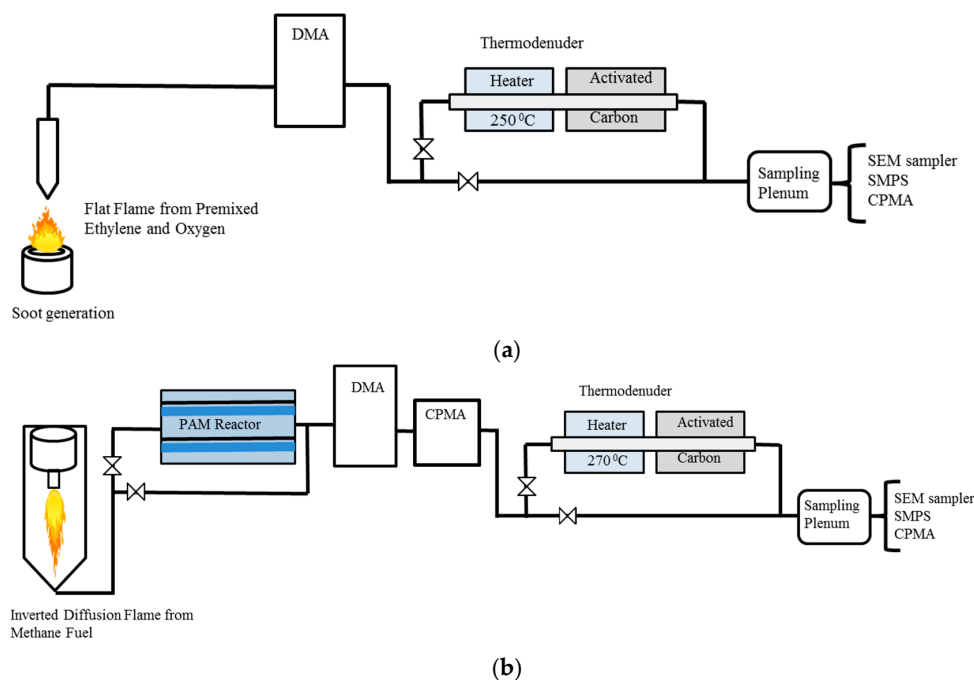


Figure 1. Soot generation and sampling set-ups in (a) Boston College Experiment 2 (BC2) and (b) Boston College Experiment 4 (BC4).

In addition, we selected two sets of soot samples generated during BC4 from the combustion of methane in an inverted diffusion flame burner (methane and O_2 mixture) at a $d_m = 253$ nm and 252 nm for nascent and $d_m = 253$ nm, and 251 nm for the corresponding denuded soot particles. The global ϕ for both sample sets was about 0.7, but the actual value of ϕ is unknown. In the diffusion flame, the fuel burns in excess of air making the value of ϕ less than 1. Effluent from the flame burner was passed through separate annular denuders loaded with molecular sieves and activated charcoal to remove water vapor and volatile organic compounds from the sample flow. As in BC2, a Huffman TD (heating section set at 270°C) was used to remove the volatile components. For both experiments, the sample flow rate through the TD was 2 LPM, resulting in a residence time of 5 s in the heating section and 4 s in the denuder section. During BC4, unlike during BC2, particles were first mobility size selected by a Differential Mobility Analyzer (DMA) (TSI Inc., Saint Paul, MN, USA) and the mass was selected by a Centrifugal Particle Mass Analyzer (CPMA) (Cambustion Ltd., Cambridge, UK) before thermodenuding. The first set of samples consisted of nascent and nascent-denuded soot, while the second set consisted of nascent-oxidized and nascent-oxidized-denuded soot. Soot was oxidized by exposure to ozone (O_3) and hydroxyl (OH) radicals in a Potential Aerosol Mass (PAM) oxidation flow reactor [54], at input O_3 and H_2O mixing ratios of ~ 15 ppm and $\sim 1\%$, and UV actinic flux $\sim 2 \times 10^{12}$ ph $\text{cm}^{-2} \text{s}^{-1}$ ($\lambda = 254$ nm). These operating conditions correspond to an integrated OH exposure of approximately 2×10^{12} molec $\text{cm}^{-3} \text{s}$ [55], and likely generate highly oxygenated organic molecules, such as carboxylic acids on the surface of the nascent-oxidized soot particles [56]. The nascent-oxidized soot was thermo-denuded at a temperature of 270°C . The set of nascent-oxidized soot samples was included here to investigate if the thermodenuding effect is different for nascent

versus nascent-oxidized soot. During BC4, soot particles were collected on 13 mm diameter Nuclepore filters having a pore size of 0.1 μm diameter (Whatman Inc., Chicago, IL, USA).

All the filters were coated with 1.8 ($\pm 10\%$) nm thick layer of Pt/Pd alloy in a sputter coater (Hummer[®] 6.2, Anatech USA, Union city, CA, USA) and imaged with a field emission scanning electron microscope (FE-SEM) (Hitachi S-4700, Tokyo, Japan). From the FE-SEM images, several morphological parameters were evaluated [6] using the image processing software ImageJ (National Institutes of Health, Bethesda, MD, USA) [57].

2.2. Soot Morphological Parameters

As mentioned in the introduction, soot particles are aggregates of monomers that exhibit scale-invariant fractal structures [58,59]. Soot aggregates can therefore be characterized by a fractal dimension (D_f), in which the mass of the aggregate M (proportional to the number of monomers N in the aggregate) scales with the ratio of the radius of gyration (R_g) to the radius of the monomers (R_p), as in M (or N) $\propto (R_g/R_p)^{D_f}$ [60]. D_f is a commonly used parameter to quantify the soot morphology. Lacy soot particles have low D_f values, while compact soot particles have higher D_f values. The D_f of an ensemble of soot particles can be calculated by plotting N vs. R_g (or a surrogate for it). N scales with R_g as a power law with exponent D_f [61]:

$$N = k_g \left(\frac{R_g}{R_p} \right)^{D_f} \quad (1)$$

where k_g is a pre-factor whose value depends on the overlap between the monomers in the aggregate. The relation formulated by Köylü et al. [61] was used to estimate D_f with the geometric mean diameter of the aggregate, \sqrt{LW} , as a surrogate for $2R_g$:

$$N = k_{LW} \left(\frac{\sqrt{LW}}{2R_p} \right)^{D_f} \quad (2)$$

where L is the maximum length and W is the maximum width (orthogonal to L), K_{LW} is a prefactor and R_p is calculated from the mean of the projected area of the monomer. In general, it is difficult to measure N using an SEM image alone, because only two-dimensional (2-D) projections of the soot particles are typically available. Therefore, N is often estimated from the projected area of the soot aggregate A_p and the mean projected area of the monomers A_m using the relation provided by Oh and Sorensen [62]:

$$N = k_a \left(\frac{A_p}{A_m} \right)^\alpha \quad (3)$$

where α and k_a are constants that depend on the overlap between monomers in the 2-D projected image of the particle. In our case, we used $K_a = 1.15$ and $\alpha = 1.09$ for all of our nascent and nascent-denuded soot aggregates [61]. This selection of K_a and α values is reasonable since we only studied nascent soot particles that are minimally coated.

In addition to D_f , several other 2-D morphological parameters were calculated from the FE-SEM images to investigate potential changes due to thermodenuding. The calculated parameters included roundness, convexity, aspect ratio (AR), and area equivalent diameter (D_{Aeq}). Figure 2a shows the definition of some of these parameters. D_{Aeq} is the diameter of a spherical particle with a projected area equivalent to the projected area of the aggregate. Roundness is calculated from the ratio of the projected area of the aggregate to the area of the circle having a diameter equal to the maximum projected length L , and fully inscribing the projected image of the aggregate (Figure 2b). Convexity (sometimes termed solidity) is the ratio of the projected area of the particle to the area of the smallest convex hull polygon, in which the 2-D projection of the aggregate is inscribed (Figure 2c). AR is calculated as the ratio of L to W . Higher values of roundness and convexity or lower AR often corresponds to more compact

soot particles. However, it has to be noted that D_f , roundness and convexity are parameters with very different meanings and definitions. The first is a scaling factor, the second is a geometric property, and the third is a measure of the particle topology. That is why we investigated all of these three parameters to characterize the morphology of soot rather than looking at a single one. We analyzed a total of 1223 images of individual soot particles.

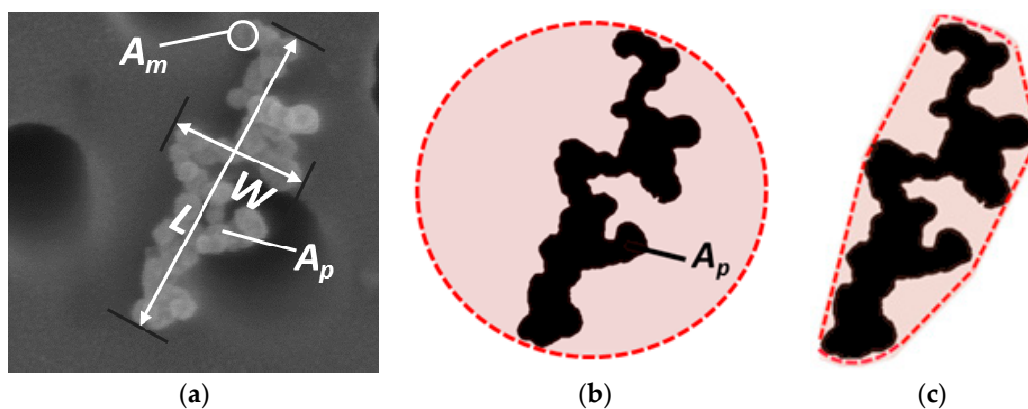


Figure 2. (a) Example of SEM image of a soot particle showing the definition of several parameters measured from the projected image: maximum projected length L , maximum projected width W , projected area of monomer A_m and projected area of particle A_p . (b) Schematic representation of the roundness calculation for the same soot particle shown in (a). (c) Schematic representation of the convexity calculation for the same soot particle shown in (a). The pink shades in (b,c) represent the equivalent area for a circle and the convex hull, respectively, for the binary image of the soot particle shown in (a).

3. Results and Discussion

As mentioned earlier, we analyzed images from four sets of nascent and nascent-denuded soot sample pairs of different sizes and a fifth set of nascent-oxidized denuded soot. Examples of images of soot particles before and after thermodenuding are shown in Figure 3.

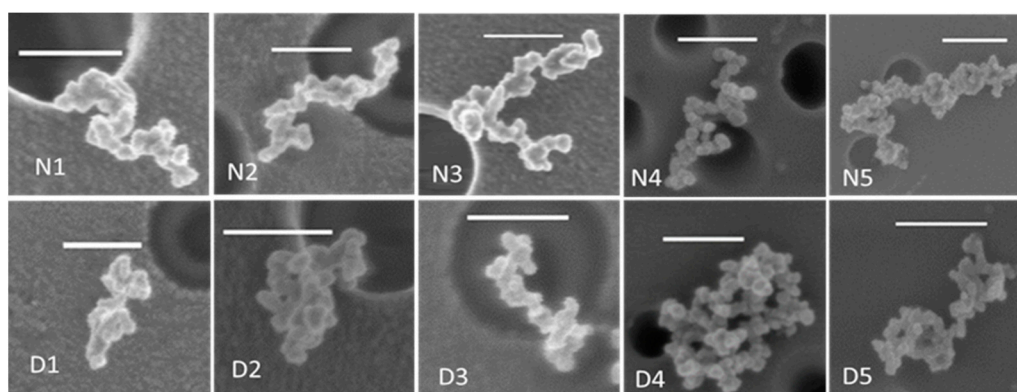


Figure 3. SEM micrographs of nascent (N) and thermodenuded (D) soot particles. The white horizontal bar in each micrograph represents a length scale of 200 nm. Dark circles are the holes in the filter.

$N1$, $N2$, $N3$, and $N4$ are four differently sized nascent soot samples and $D1$, $D2$, $D3$, and $D4$ are the corresponding nascent-denuded sets. $N5$ - $D5$ is a pair of nascent-oxidized soot before and after thermodenuding. Table 1 summarizes the features of the analyzed soot particles. Sets $N1$ - $D1$, $N2$ - $D2$, and $N3$ - $D3$ are the three sets from BC2, while sets $N4$ - $D4$, and $N5$ - $D5$ are from BC4.

Table 1. Summary of physical and morphological parameters for the soot particles analyzed.

Experiment	Statistics	BC2				BC4					
Sample		N1	D1	N2	D2	N3	D3	N4	D4	N5	D5
Fuel type		E	E	E	E	E	E	M	M	M	M
#Particles analyzed		108	151	113	163	114	109	113	105	122	125
N	Mean	41	55	121	104	110	153	158	188	155	166
	S.D	16	26	65	53	44	90	96	87	75	106
	S.E	2	2	6	4	4	9	9	8	7	9
d_m (nm)	Mean	153	151	181	175	250	241	253	253	252	251
	Mean	1.02	0.78	1.52	1.08	2.85	2.20	2.37	2.34	2.41	2.18
	S.D.	(0.03)	(0.03)	(0.05)	(0.04)	(0.14)	(0.13)	(0.11)	(0.13)	(0.11)	(0.11)
D_f	Fit slope	1.86	1.84	1.73	1.72	1.78	1.79	1.80	1.76	1.65	1.80
	S.E.	(0.05)	(0.04)	(0.05)	(0.06)	(0.08)	(0.05)	(0.05)	(0.06)	(0.05)	(0.05)
K_g	Fit intercept	1.78	1.98	2.50	2.50	2.22	2.00	2.10	2.56	2.87	2.16
	S.E.	(0.04)	(0.03)	(0.05)	(0.05)	(0.08)	(0.06)	(0.06)	(0.07)	(0.06)	(0.06)
d_p (nm)	Mean	33.5	31.8	26.8	25.7	32.1	30.3	23.5	22.8	23.9	23.1
	Median	33.5	32.4	26.5	25.9	32.1	28.9	23.2	22.5	23.7	23.0
	S.D.	(2.1)	(3.3)	(2.7)	(2.6)	(2.1)	(6.9)	(3.1)	(2.2)	(2.5)	(3.4)
	S.E.	(0.21)	(0.27)	(0.26)	(0.21)	(0.20)	(0.66)	(0.30)	(0.22)	(0.23)	(0.31)
Roundness	Mean	0.41	0.43	0.36	0.34	0.38	0.31	0.31	0.35	0.33	0.33
	Median	0.42	0.42	0.35	0.35	0.35	0.30	0.30	0.34	0.32	0.31
	S.D.	(0.12)	(0.12)	(0.11)	(0.10)	(0.12)	(0.09)	(0.11)	(0.12)	(0.11)	(0.11)
	S.E.	(0.01)	(0.01)	(0.01)	(0.01)	(0.01)	(0.01)	(0.01)	(0.01)	(0.01)	(0.01)
Convexity	Mean	0.72	0.75	0.66	0.66	0.62	0.59	0.61	0.66	0.61	0.63
	Median	0.73	0.74	0.66	0.65	0.62	0.58	0.61	0.66	0.61	0.62
	S.D.	(0.09)	(0.08)	(0.09)	(0.10)	(0.09)	(0.10)	(0.10)	(0.11)	(0.12)	(0.11)
	S.E.	(0.01)	(0.01)	(0.01)	(0.01)	(0.01)	(0.01)	(0.01)	(0.01)	(0.01)	(0.01)
D_{Aeq} (nm)	Mean	169	181	220	196	255	262	215	230	219	214
	Median	171	175	208	189	262	260	199	220	213	202
	S.D.	(33)	(35)	(55)	(41)	(46)	(49)	(54)	(56)	(50)	(59)
	S.E.	(3)	(3)	(5)	(3)	(4)	(5)	(5)	(5)	(5)	(5)
AR	Mean	1.79	1.73	1.84	1.92	1.78	1.85	1.99	1.95	1.85	1.88
	Median	1.66	1.62	1.70	1.78	1.68	1.72	1.85	1.82	1.80	1.83
	S.D.	(0.51)	(0.42)	(0.49)	(0.51)	(0.57)	(0.50)	(0.60)	(0.60)	(0.50)	(0.50)
	S.E.	(0.05)	(0.03)	(0.05)	(0.04)	(0.05)	(0.05)	(0.06)	(0.06)	(0.05)	(0.04)

In Table 1, E = ethylene and M = methane represent the fuel type. N is the average number of monomers per aggregate, estimated in each sample using Equation (3). K_g values have been estimated using the relation $K_g = K_{LW} \cdot (1.17)^{D_f}$ where $\sqrt{LW}/2R_g = 1.17$ has been taken from Köylü et al. [61] and the values of K_{LW} and D_f have been calculated from a log-log plot using Equation (2). d_p is the mean diameter of the monomers in an aggregate, d_m is the mean mobility diameter (in nm) and M_{CPMA} represents the mean mass of the particle (in fg) as measured by the CPMA. For D_f the term in parenthesis is the standard error (S.E.) calculated from the power fit using Equation (2), for the other quantities, it is the S.E. (standard deviation of the mean) and the standard deviation (S.D.).

The largest decrease in the mean value of d_p (by 5.6%) after thermodenuding is found for the N3-D3 set. The decrease in d_p could be due to the partial removal of material volatile at the TD temperature and present on the nascent soot. A decrease in the monomer size after thermal treatment was previously observed when soot samples were heated at higher temperatures (400–900 °C) due to the removal of a part of the nascent PAH layers from the monomers surface [63]. Also, the mean d_p size, as well as the differences in the mean values of d_p after thermodenuding are smaller for the inverted diffusion flame with respect to those of the McKenna flame. These changes suggest that there was less volatile material present in the nascent soot generated from the inverted flame. This effect could be due to the different type of fuel, as well as different ϕ . In a study of ethylene flame generated soot from a McKenna burner, the size of d_p in thermodenuded soot particles was found larger for higher ϕ [64]. This is consistent with the study by Ghazi and Olfert [16] that generated soot by an inverted diffusion flame and found no measurable amount of volatile material when the mass was measured after thermodenuding. While, Slowik et al. [64], using a McKenna flame, found that thermodenuding removed only about 0.05 mass fraction of volatile material for the nascent soot containing 0.1 mass fraction of non-refractory material (at $\phi = 2.1$) from an ethylene flat flame.

To investigate whether the soot aggregates restructured after thermodenuding, we first analyze the changes in D_f as summarized in Figure 4.

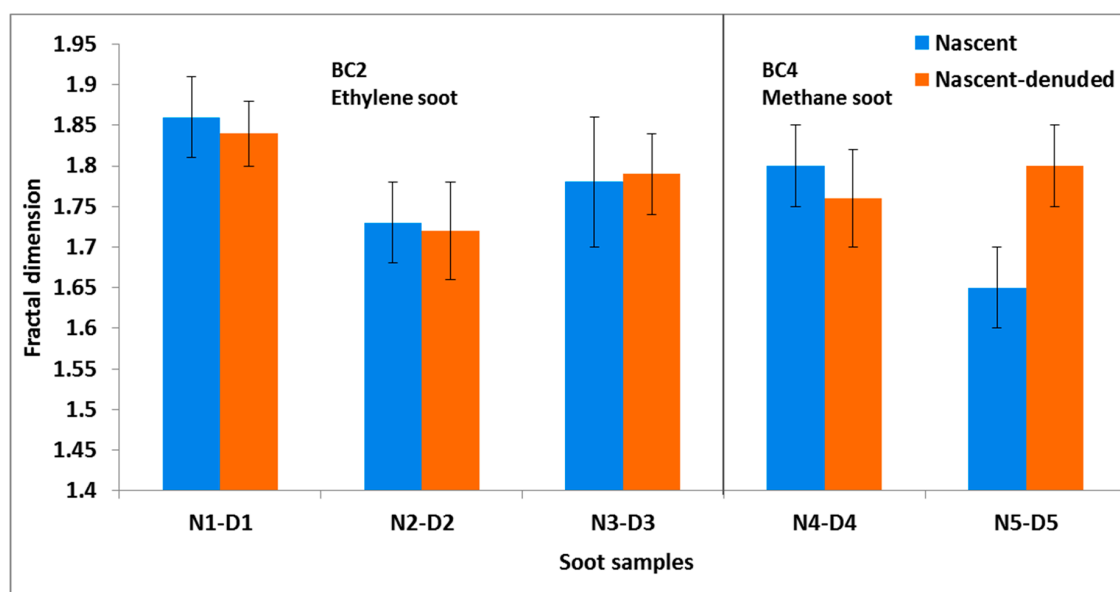


Figure 4. Fractal dimension of nascent (in blue) and nascent-denuded (in orange) soot pairs of different mobility sizes. The error bars represent the standard errors.

For all five sample sets, D_f lies between 1.65 and 1.86 (Table 1). The derivation of D_f and plots for all of the samples are shown in the supplementary material (Figure S1). These values of D_f are in agreement with the observations made in previous studies on nascent soot particles produced from different fuel sources [3,65]. Also for all nascent vs. denuded pairs (except for the nascent-oxidized pair: N5-D5), there is no significant change (within 1σ) in D_f after thermodenuding (Figure 4). For the N5-D5 pair, the D_f changes by about 9% (from 1.65 to 1.80), whereas for all other cases, the change is less than 2.3%. The CPMA data for the BC4 sample shows that the mass decreased from 2.37 to 2.34 fg for nascent soot, while for the nascent-oxidized soot of the same mobility size, the mass decreased from 2.41 to 2.18 fg after thermodenuding. The larger decrease in mass for the nascent oxidized soot suggests that the coating material on the oxidized soot was removed during thermodenuding. A possible explanation for the increase of D_f after thermodenuding the oxidized soot might be that the soot structure was slightly modified during the evaporation of the coating material. Interestingly, for the BC2 soot samples, there is no significant change in D_f despite the significant change in mass (up to ~29%) of soot after thermodenuding (see CPMA data in Table 1). This result suggests that for the BC2 sample sets, the removal of the coating present on nascent soot did not affect the structure of soot. This is most probably due to the chemical composition of the organics that were removed by TD. This result is consistent with the thermodenuding experiment of uncoated soot (fractal soot generated at lower $\varnothing = 2.1$) by Slowik et al. [64] that found no change in D_f (derived from mass-mobility relation in their case) after denuding. They suggested that the removal of organics from the uncoated soot during denuding cannot change the skeletal framework of soot. Cross et al. [9] observed only minor restructuring of soot when dioctyl sebacate coating was removed by thermodenuding, suggesting that the removal of organic coating may have little impact on the restructuring of soot. For soot from a flat flame burner, Slowik et al. [66] found that the organic carbon (OC) content (mass fraction of 0.1) was composed of a comparable amount of aliphatic and aromatic compounds at a lower \varnothing ($\varnothing = 1.85$), but at a higher \varnothing ($\varnothing > 4$), the OC content (mass fraction of 0.55) had only a minor fraction of aliphatic compounds. We thus hypothesize that the nascent organics on the soot from the BC2 experiments considered here consisted in a large fraction of aliphatic compounds.

To account for the mass change after thermodenuding on the coating of soot particle, we calculated coating thickness (ΔR_{ve}) in terms of volume equivalent radius (R_{ve}). The difference between the volume equivalent radius of nascent soot and the thermodenuded soot particle was used to estimate the thickness of the coating material. For the case of maximum mass loss ($\sim 29\%$), coating thickness was estimated to be 8.4 nm. (See supplementary material for the calculation).

To further investigate possible morphological changes after thermodenuding, we studied the convexity and roundness of soot particles for all five sample sets. The maximum change in the mean value of roundness occurs for set *N3-D3* (about 18%), followed by the set *N4-D4* (about 13%). For the other sets, the mean value of roundness changes by less than 10%. For the case of convexity, the maximum change in the mean value occurs for set *N4-D4* (about 8%). For all other sets, the mean value of convexity changes by less than 5%. The larger changes in roundness and convexity for these sample sets are statistically significant (at 1σ) although still minor.

We should point out, however, that image acquisition conditions (e.g., due to different magnifications, scan rates or over/under focusing) and image processing biases (e.g., image thresholding) can introduce additional errors in roundness, convexity, and D_f . In some cases, these errors are larger than the statistical errors provided in Table 1. To quantify these uncertainties, we acquired multiple images of six individual particles (from sample *N5*) and processed them under different conditions, as mentioned above. We estimated the uncertainties due to image acquisition and image processing biases in roundness and convexity to be 0.01 and 0.02, respectively. Similarly, uncertainties in N and d_p were estimated to be 16% and 13% (3.4 nm), respectively, which resulted in an error of 0.08 in D_f .

In Figure 5a,b we show box and whisker plots for the convexity and the roundness, respectively of the soot particles before and after thermodenuding. The convexity ranges from 0.37 to 0.91, while the roundness ranges from 0.09 to 0.75 (see Table 1 for details). No substantial changes in roundness or convexity are evident after thermodenuding.

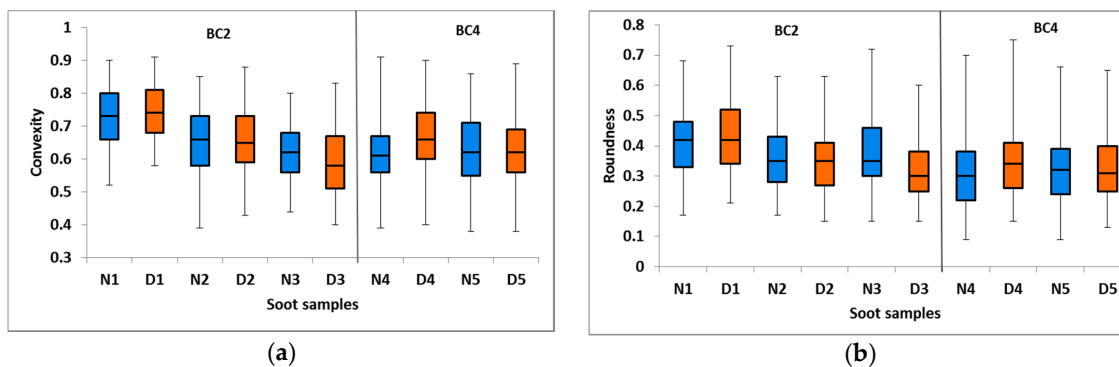


Figure 5. Box and whisker plots of (a) convexity and (b) roundness. Blue boxes represent the nascent soot and orange boxes represent the nascent-denuded soot. The horizontal bar inside the box represents the median value while the lower part and upper part of the box separated by the horizontal bar represent the first and third quartiles, respectively. The lower and upper extremities of the whiskers represent the minimum and maximum values, respectively.

In Figure 6, we show the probability distributions of convexity and roundness for all nascent and denuded soot pairs. The solid and the dashed lines represent the mean values for nascent and denuded soot, respectively, while the shaded color bands in blue and orange represent one standard deviation. These means and uncertainty bands were calculated with a bootstrap approach, resampling with replacement from the raw data and constructing 100,000 frequency distributions [67].

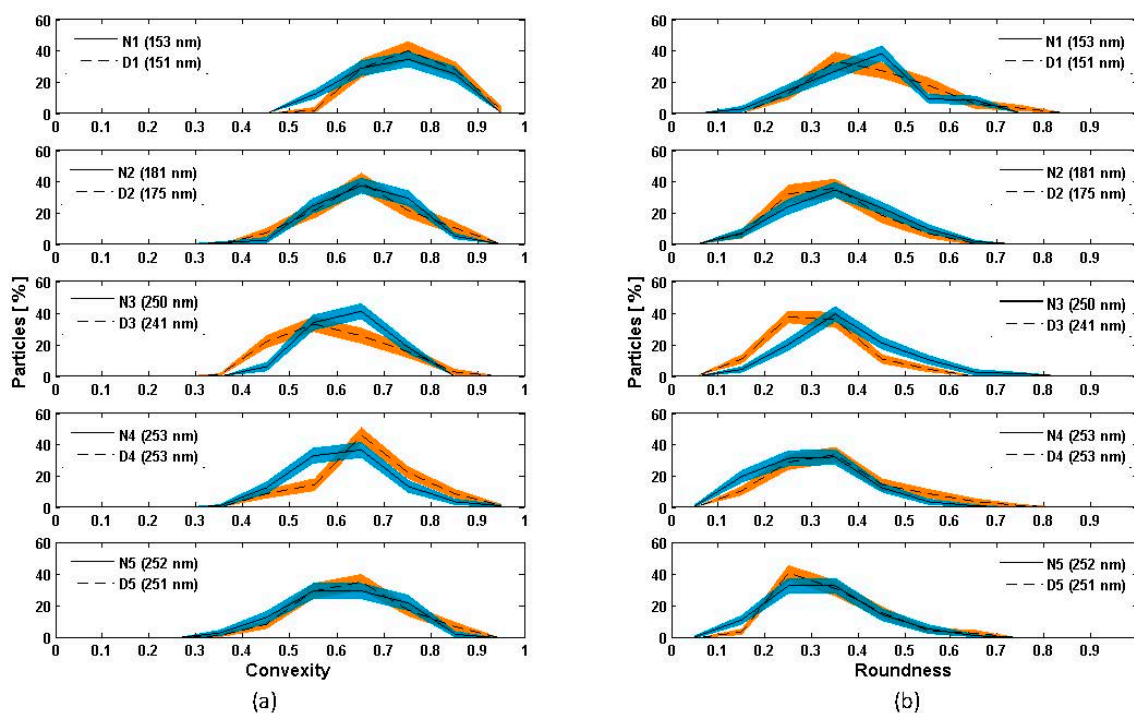


Figure 6. Distributions of (a) convexity and (b) roundness for nascent and nascent-denuded soot particles of different sizes (the mobility diameter is reported in parenthesis in the legends).

For the $N3$ - $D3$ pair, the distribution of convexity and roundness peaks at slightly lower values after thermodenuding. The convexity of particles decreases slightly with the increasing value of the mobility diameter for both nascent and denuded particles. This suggests that the smaller soot particles are more compact when compared to larger particles, in agreement with previous studies [68,69]. Figure 6a also suggests that for smaller mobility diameters, the convexity of soot from the ethylene diffusion flame might be less affected by thermodenuding as compared to the larger sized particles. With the methane diffusion flame ($N4$ - $D4$ and $N5$ - $D5$ sets) particles showed negligible changes in roundness and convexity after thermodenuding, for both nascent and nascent-oxidized soot (Figure 6a $N4$ - $D4$ and $N5$ - $D5$, respectively).

For completeness, we also investigated the changes in AR and D_{Aeq} . Both show only small changes after thermodenuding (Table 1). Our observations on the five sets of soot pairs show only minor changes in the morphology of nascent soot after thermodenuding.

To study the potential effect of PAM on nascent soot prior to thermodenuding, we compared the parameters between $N4$ (nascent soot without oxidation in PAM) and $N5$ (nascent soot with oxidation in PAM) samples. $N4$ and $N5$ have comparable masses of 2.37 fg and 2.41 fg, respectively, and a similar mobility diameter \sim 250 nm. A total of 113 and 122 individual soot particles were analyzed for $N4$ and $N5$, respectively. Both samples show nearly the same number of monomers in the soot particles imaged. $N4$ has 158 and $N5$ has 155 monomers on average. Also, the mean diameter of monomers is similar in the two samples, 23.5 nm for $N4$ and 23.9 nm for $N5$. The similar key properties of the soot particles in the two experiments suggest that $N4$ and $N5$ are suitable samples to make a comparison of nascent soot experiments with and without PAM reactor without thermodenuding.

The roundness for $N4$ (0.31) and for $N5$ (0.33) and the convexity (0.61 for both $N4$ and $N5$) are within the error bars. However, D_f for $N5$ (1.65) is smaller than for $N4$ (1.80). The value of D_f for $N5$ is somehow smaller than the values typically found for nascent soot (1.7–1.9), but lie within the limit when the imaging and thresholding uncertainties discussed above are added in quadrature to the statistical errors. However, in the downstream of the thermodenuder, $D5$ and $D4$ (samples with and without PAM treatment, respectively) show comparable values of roundness (0.35 for $D4$ and 0.33

for D_5), convexity (0.66 for D_4 , and 0.63 for D_5), and D_f (1.76 for D_4 and 1.80 for D_5). Since we have only one set for the nascent-oxidized soot, we are unable to draw a firm conclusion on the effect of thermodenuding on such particles. Although at the time, we have no clear explanation for the minor difference in D_f , it is possible that the different nanophysical properties of the nascent-oxidized soot might indeed result in a higher sensitivity to thermodenuding.

From a study of young and mature soot particles under high-resolution transmission electron microscopy (HRTEM), Alfè et al. [70] found no significant difference in the nanostructure of soot monomers. In addition, they found that the change in the H/C ratio is smaller for methane soot when compared to that of other fuels. In another study, Vander Wal and Tomasek [71], also using HRTEM, reported that the oxidation rate of nascent soot depends upon the nanostructure, for example, the length of graphene segments, curvature, and its orientation. Ishiguro et al. [72], Song et al. [73], Müller et al. [74], also showed a relation between the monomers nanostructure and the soot oxidation from different fuel sources. Other studies showed negligible influence of ozone on soot oxidation [75,76], as compared to the OH radical. In another study of soot oxidation [77], both the ozone and OH at atmospherically relevant levels were found to have no effect on the oxidation of the elemental carbon (EC) fraction in soot. In our case, the CPMA data showed that the main fraction (>90%) of methane-generated soot consisted of EC, suggesting that the oxidation in the PAM chamber might have a negligible effect on the overall morphology of soot.

In a study on the fragmentation and bond strength of diesel soot, Rothenbacher et al. [53] made a comparison between nascent soot treated with and without a TD as a function of impact velocity, and found no substantial change in the degree of fragmentation of nascent soot aggregates due to the thermodenuding. A low-pressure impactor was used to impart velocities of up to 300 m/s to the soot particles. The TD used in their study had a residence time of 0.43 s, and the sample was heated to 280 °C. In another study by Raj et al. [63], soot fragmentation was observed after thermodenuding in the temperature range of 400–900 °C on diesel soot and commercial soot (Printex-U). However, in the lower temperature range, below 500 °C, they found a minor effect on soot fragmentation. Bambha et al. [26] noticed only a small effect of thermodenuding at 410 °C (transit time of ~34 s) on the morphology of soot during the removal of oleic acid coating. In another study, Slowik et al. [64] did not observe any measurable change in the structure of soot when fresh soot (generated at $\varnothing = 2.1$ and 3.5) was thermodenuded at 200 °C. Our results of the negligible or minor restructuring of thermodenuded soot particles are in agreement with these previous studies suggesting that these results are robust and reproducible.

4. Conclusions

In this study, we used scanning electron microscopy to investigate the morphology of nascent soot aggregates prior to, and after, thermodenuding in a low-temperature regime (<270 °C). Despite mass losses of up to ~29% in the nascent soot (removal of ~8 nm coating layer from the soot surface), we detected only minor effects on the soot structure after thermodenuding, irrespective of the fuel type and particle size. We observed no significant change in the fractal dimension, although roundness and convexity showed some minor changes in our case. Future work should focus on the effect on the structure of nascent soot of higher thermodenuding temperatures.

Supplementary Materials: The following are available online at www.mdpi.com/2073-4433/8/9/166/s1, Figure S1: Plots of fractal dimension of nascent-denuded soot pairs. The solid line and dashed line in each plot represent the slope for nascent and denuded soot respectively.

Acknowledgments: This work was supported in part by the Office of Science (BER), Department of Energy (Atmospheric System Research) Grant no. DE-SC0011935 and no. DE-SC0010019, and the Atmospheric Chemistry program of the National Science Foundation Grant no. AGS-1536939 to Boston College, 1537446 to Aerodyne Research Inc. S. China was partially supported by a NASA Earth and Space Science Graduate Fellowships no. NNX12AN97H.

Author Contributions: This manuscript describes the analysis of soot samples obtained in two experimental projects performed in the laboratories of Paul Davidovits at Boston College. Paul Davidovits and Tim Onasch

participated in the planning, setting up and supervising of BC2 and BC4. Adam Ahern and Jason Olfert assisted in the experimental design and the experiments. Tim Onasch and Eben Cross led the BC2 experiments including operation of all experimental aspects of the project and analysis of the SMPS and CPMA data used here. Tim Onasch, Lindsay Wolff and Andrew Lambe led the BC4 experiment including operation of all experimental aspects of the project. Swarup China and Claudio Mazzoleni collected the samples during BC4 and BC2, respectively. Manvendra Dubey participated in the experiments and provided the instrumentation used for sampling during BC2. Janarjan Bhandari and Swarup China performed the SEM analysis. Janarjan Bhandari, Claudio Mazzoleni and Swarup China wrote most of the paper with significant contributions and edits from all the coauthors.

Conflicts of Interest: The authors declare no conflict of interest.

References

- Haynes, B.S.; Wagner, H.G. Soot formation. *Prog. Energy Combust. Sci.* **1981**, *7*, 229–273. [[CrossRef](#)]
- Buseck, P.R.; Adachi, K.; Gelencsér, A.; Tompa, É.; Pósfai, M. Ns-soot: A material-based term for strongly light-absorbing carbonaceous particles. *Aerosol Sci. Technol.* **2014**, *48*, 777–788. [[CrossRef](#)]
- Sorensen, C. Light scattering by fractal aggregates: A review. *Aerosol Sci. Technol.* **2001**, *35*, 648–687. [[CrossRef](#)]
- Adachi, K.; Buseck, P. Internally mixed soot, sulfates, and organic matter in aerosol particles from Mexico city. *Atmos. Chem. Phys.* **2008**, *8*, 6469–6481. [[CrossRef](#)]
- Bambha, R.; Dansson, M.A.; Schrader, P.E.; Michelsen, H.A. *Effects of Volatile Coatings on the Morphology and Optical Detection of Combustion-Generated Black Carbon Particles*; Sandia National Laboratories (SNL-CA): Livermore, CA, USA, 2013. Available online: <http://prod.sandia.gov/techlib/access-control.cgi/2013/137660.pdf> (accessed on 27 July 2017).
- China, S.; Salvadori, N.; Mazzoleni, C. Effect of traffic and driving characteristics on morphology of atmospheric soot particles at freeway on-ramps. *Environ. Sci. Technol.* **2014**, *48*, 3128–3135. [[CrossRef](#)] [[PubMed](#)]
- Park, K.; Kittelson, D.B.; McMurry, P.H. Structural properties of diesel exhaust particles measured by transmission electron microscopy (TEM): Relationships to particle mass and mobility. *Aerosol Sci. Technol.* **2004**, *38*, 881–889. [[CrossRef](#)]
- China, S.; Scarnato, B.; Owen, R.C.; Zhang, B.; Ampadu, M.T.; Kumar, S.; Dzepina, K.; Dziobak, M.P.; Fialho, P.; Perlinger, J.A.; et al. Morphology and mixing state of aged soot particles at a remote marine free troposphere site: Implications for optical properties. *Geophys. Res. Lett.* **2015**, *42*, 1243–1250. [[CrossRef](#)]
- Cross, E.S.; Onasch, T.B.; Ahern, A.; Wrobel, W.; Slowik, J.G.; Olfert, J.; Lack, D.A.; Massoli, P.; Cappa, C.D.; Schwarz, J.P.; et al. Soot particle studies—Instrument inter-comparison—project overview. *Aerosol Sci. Technol.* **2010**, *44*, 592–611. [[CrossRef](#)]
- Adachi, K.; Chung, S.H.; Buseck, P.R. Shapes of soot aerosol particles and implications for their effects on climate. *J. Geophys. Res. Atmos.* **2010**, *115*, D15. [[CrossRef](#)]
- China, S.; Mazzoleni, C.; Gorkowski, K.; Aiken, A.C.; Dubey, M.K. Morphology and mixing state of individual freshly emitted wildfire carbonaceous particles. *Nat. Commun.* **2013**, *4*, 2122. [[CrossRef](#)] [[PubMed](#)]
- Healy, R.M.; Wang, J.M.; Jeong, C.H.; Lee, A.K.; Willis, M.D.; Jaroudi, E.; Zimmerman, N.; Hilker, N.; Murphy, M.; Eckhardt, S.; et al. Light-absorbing properties of ambient black carbon and brown carbon from fossil fuel and biomass burning sources. *J. Geophys. Res. Atmos.* **2015**, *120*, 6619–6633. [[CrossRef](#)]
- Liu, S.; Aiken, A.C.; Gorkowski, K.; Dubey, M.K.; Cappa, C.D.; Williams, L.R.; Herndon, S.C.; Massoli, P.; Fortner, E.C.; Chhabra, P.S.; et al. Enhanced light absorption by mixed source black and brown carbon particles in UK winter. *Nat. Commun.* **2015**, *6*, 8435. [[CrossRef](#)] [[PubMed](#)]
- Zhang, R.; Khalizov, A.F.; Pagels, J.; Zhang, D.; Xue, H.; McMurry, P.H. Variability in morphology, hygroscopicity, and optical properties of soot aerosols during atmospheric processing. *Proc. Natl. Acad. Sci. USA* **2008**, *105*, 10291–10296. [[CrossRef](#)] [[PubMed](#)]
- Adachi, K.; Buseck, P.R. Changes of ns-soot mixing states and shapes in an urban area during CalNex. *J. Geophys. Res. Atmos.* **2013**, *118*, 3723–3730. [[CrossRef](#)]
- Ghazi, R.; Olfert, J. Coating mass dependence of soot aggregate restructuring due to coatings of oleic acid and dioctyl sebacate. *Aerosol Sci. Technol.* **2013**, *47*, 192–200. [[CrossRef](#)]

17. Jacobson, M.Z. Strong radiative heating due to the mixing state of black carbon in atmospheric aerosols. *Nature* **2001**, *409*, 695–697. [[CrossRef](#)] [[PubMed](#)]
18. Lack, D.; Cappa, C. Impact of brown and clear carbon on light absorption enhancement, single scatter albedo and absorption wavelength dependence of black carbon. *Atmos. Chem. Phys.* **2010**, *10*, 4207–4220. [[CrossRef](#)]
19. Liu, D.; Taylor, J.W.; Young, D.E.; Flynn, M.J.; Coe, H.; Allan, J.D. The effect of complex black carbon microphysics on the determination of the optical properties of brown carbon. *Geophys. Res. Lett.* **2015**, *42*, 613–619. [[CrossRef](#)]
20. Schnitzler, E.G.; Dutt, A.; Charbonneau, A.M.; Olfert, J.S.; Jäger, W. Soot aggregate restructuring due to coatings of secondary organic aerosol derived from aromatic precursors. *Environ. Sci. Technol.* **2014**, *48*, 14309–14316. [[CrossRef](#)] [[PubMed](#)]
21. Van Poppel, L.H.; Friedrich, H.; Spinsby, J.; Chung, S.H.; Seinfeld, J.H.; Buseck, P.R. Electron tomography of nanoparticle clusters: Implications for atmospheric lifetimes and radiative forcing of soot. *Geophys. Res. Lett.* **2005**, *32*, L24811. [[CrossRef](#)]
22. Westcott, S.L.; Zhang, J.; Shelton, R.K.; Bruce, N.M.; Gupta, S.; Keen, S.L.; Tillman, J.W.; Wald, L.B.; Strecker, B.N.; Rosenberger, A.T.; et al. Broadband optical absorbance spectroscopy using a whispering gallery mode microsphere resonator. *Rev. Sci. Instrum.* **2008**, *79*, 033106. [[CrossRef](#)] [[PubMed](#)]
23. Cappa, C.D.; Onasch, T.B.; Massoli, P.; Worsnop, D.R.; Bates, T.S.; Cross, E.S.; Davidovits, P.; Hakala, J.; Hayden, K.L.; Jobson, B.T.; et al. Radiative absorption enhancements due to the mixing state of atmospheric black carbon. *Science* **2012**, *337*, 1078–1081. [[CrossRef](#)] [[PubMed](#)]
24. Fuller, K.A.; Malm, W.C.; Kreidenweis, S.M. Effects of mixing on extinction by carbonaceous particles. *J. Geophys. Res. Atmos.* **1999**, *104*, 15941–15954. [[CrossRef](#)]
25. Khalizov, A.F.; Xue, H.; Wang, L.; Zheng, J.; Zhang, R. Enhanced light absorption and scattering by carbon soot aerosol internally mixed with sulfuric acid. *J. Phys. Chem. A* **2009**, *113*, 1066–1074. [[CrossRef](#)] [[PubMed](#)]
26. Bambha, R.P.; Dansson, M.A.; Schrader, P.E.; Michelsen, H.A. Effects of volatile coatings and coating removal mechanisms on the morphology of graphitic soot. *Carbon* **2013**, *61*, 80–96. [[CrossRef](#)]
27. Lack, D.A.; Langridge, J.M.; Bahreini, R.; Cappa, C.D.; Middlebrook, A.M.; Schwarz, J.P. Brown carbon and internal mixing in biomass burning particles. *Proc. Natl. Acad. Sci. USA* **2012**, *109*, 14802–14807. [[CrossRef](#)] [[PubMed](#)]
28. Xue, H.; Khalizov, A.F.; Wang, L.; Zheng, J.; Zhang, R. Effects of coating of dicarboxylic acids on the mass–mobility relationship of soot particles. *Environ. Sci. Technol.* **2009**, *43*, 2787–2792. [[CrossRef](#)] [[PubMed](#)]
29. Huffman, J.A.; Ziemann, P.J.; Jayne, J.T.; Worsnop, D.R.; Jimenez, J.L. Development and characterization of a fast-stepping/scanning thermodesorber for chemically-resolved aerosol volatility measurements. *Aerosol Sci. Technol.* **2008**, *42*, 395–407. [[CrossRef](#)]
30. Wehner, B.; Philippin, S.; Wiedensohler, A. Design and calibration of a thermodesorber with an improved heating unit to measure the size-dependent volatile fraction of aerosol particles. *J. Aerosol Sci.* **2002**, *33*, 1087–1093. [[CrossRef](#)]
31. Swanson, J.; Kittelson, D. Evaluation of thermal desorber and catalytic stripper methods for solid particle measurements. *J. Aerosol Sci.* **2010**, *41*, 1113–1122. [[CrossRef](#)]
32. Knox, A.; Evans, G.; Brook, J.; Yao, X.; Jeong, C.H.; Godri, K.; Sabaliauskas, K.; Slowik, J. Mass absorption cross-section of ambient black carbon aerosol in relation to chemical age. *Aerosol Sci. Technol.* **2009**, *43*, 522–532. [[CrossRef](#)]
33. Khalizov, A.F.; Lin, Y.; Qiu, C.; Guo, S.; Collins, D.; Zhang, R. Role of OH-initiated oxidation of isoprene in aging of combustion soot. *Environ. Sci. Technol.* **2013**, *47*, 2254–2263. [[CrossRef](#)] [[PubMed](#)]
34. Chow, J.C.; Watson, J.G.; Chen, L.W.A.; Arnott, W.P.; Moosmüller, H.; Fung, K. Equivalence of elemental carbon by thermal/optical reflectance and transmittance with different temperature protocols. *Environ. Sci. Technol.* **2004**, *38*, 4414–4422. [[CrossRef](#)] [[PubMed](#)]
35. Countess, R.J. Interlaboratory analyses of carbonaceous aerosol samples. *Aerosol Sci. Technol.* **1990**, *12*, 114–121. [[CrossRef](#)]
36. Cheng, Y.; Duan, F.K.; He, K.B.; Zheng, M.; Du, Z.Y.; Ma, Y.L.; Tan, J.H. Intercomparison of thermal–optical methods for the determination of organic and elemental carbon: Influences of aerosol composition and implications. *Environ. Sci. Technol.* **2011**, *45*, 10117–10123. [[CrossRef](#)] [[PubMed](#)]

37. Khan, B.; Hays, M.D.; Geron, C.; Jetter, J. Differences in the OC/EC ratios that characterize ambient and source aerosols due to thermal-optical analysis. *Aerosol Sci. Technol.* **2012**, *46*, 127–137. [[CrossRef](#)]
38. Stanmore, B.R.; Brillhac, J.F.; Gilot, P. The oxidation of soot: A review of experiments, mechanisms and models. *Carbon* **2001**, *39*, 2247–2268. [[CrossRef](#)]
39. Ebert, M.; Inerle-Hof, M.; Weinbruch, S. Environmental scanning electron microscopy as a new technique to determine the hygroscopic behaviour of individual aerosol particles. *Atmos. Environ.* **2002**, *36*, 5909–5916. [[CrossRef](#)]
40. Ma, X.; Zangmeister, C.D.; Gigault, J.; Mulholland, G.W.; Zachariah, M.R. Soot aggregate restructuring during water processing. *J. Aerosol Sci.* **2013**, *66*, 209–219. [[CrossRef](#)]
41. Tritscher, T.; Jurányi, Z.; Martin, M.; Chirico, R.; Gysel, M.; Heringa, M.F.; DeCarlo, P.F.; Sierau, B.; Prévôt, A.S.; Weingartner, E.; et al. Changes of hygroscopicity and morphology during ageing of diesel soot. *Environ. Res. Lett.* **2011**, *6*, 034026. [[CrossRef](#)]
42. Radney, J.G.; You, R.; Ma, X.; Conny, J.M.; Zachariah, M.R.; Hodges, J.T.; Zangmeister, C.D. Dependence of soot optical properties on particle morphology: Measurements and model comparisons. *Environ. Sci. Technol.* **2014**, *48*, 3169–3176. [[CrossRef](#)] [[PubMed](#)]
43. China, S.; Kulkarni, G.; Scarnato, B.V.; Sharma, N.; Pekour, M.; Shilling, J.E.; Wilson, J.; Zelenyuk, A.; Chand, D.; Liu, S.; et al. Morphology of diesel soot residuals from supercooled water droplets and ice crystals: Implications for optical properties. *Environ. Res. Lett.* **2015**, *10*, 114010. [[CrossRef](#)]
44. Popovichcheva, O.; Persiantseva, N.; Kuznetsov, B.; Rakhmanova, T.; Shonija, N.; Suzanne, J.; Ferry, D. Microstructure and water adsorbability of aircraft combustor soots and kerosene flame soots: Toward an aircraft-generated soot laboratory surrogate. *J. Phys. Chem. A* **2003**, *107*, 10046–10054. [[CrossRef](#)]
45. Huang, P.F.; Turpin, B.J.; Pihlo, M.J.; Kittelson, D.B.; McMurry, P.H. Effects of water condensation and evaporation on diesel chain-agglomerate morphology. *J. Aerosol Sci.* **1994**, *25*, 447–459. [[CrossRef](#)]
46. Schnitzler, E.G.; Gac, J.M.; Jäger, W. Coating surface tension dependence of soot aggregate restructuring. *J. Aerosol Sci.* **2017**, *106*, 43–55. [[CrossRef](#)]
47. Leung, K.; Schnitzler, E.G.; Jaeger, W.; Olfert, J.S. Relative humidity dependence of soot aggregate restructuring induced by secondary organic aerosol: Effects of water on coating viscosity and surface tension. *Environ. Sci. Technol. Lett.* **2017**, in press. [[CrossRef](#)]
48. Weber, A.; Baltensperger, U.; Gäggeler, H.; Schmidt-Ott, A. In situ characterization and structure modification of agglomerated aerosol particles. *J. Aerosol Sci.* **1996**, *27*, 915–929. [[CrossRef](#)]
49. Weber, A.P.; Friedlander, S.K. In situ determination of the activation energy for restructuring of nanometer aerosol agglomerates. *J. Aerosol Sci.* **1997**, *28*, 179–192. [[CrossRef](#)]
50. Jang, H.D.; Friedlander, S.K. Restructuring of chain aggregates of titania nanoparticles in the gas phase. *Aerosol Sci. Technol.* **1998**, *29*, 81–91. [[CrossRef](#)]
51. Schmidt-Ott, A. New approaches to in situ characterization of ultrafine agglomerates. *J. Aerosol Sci.* **1988**, *19*, 553–563. [[CrossRef](#)]
52. Chen, C.; Fan, X.; Shaltout, T.; Qiu, C.; Ma, Y.; Goldman, A.; Khalizov, A.F. An unexpected restructuring of combustion soot aggregates by subnanometer coatings of polycyclic aromatic hydrocarbons. *Geophys. Res. Lett.* **2016**, *43*, 11080–11088. [[CrossRef](#)]
53. Rothenbacher, S.; Messerer, A.; Kasper, G. Fragmentation and bond strength of airborne diesel soot agglomerates. *Part. Fibre Toxicol.* **2008**, *5*, 9. [[CrossRef](#)] [[PubMed](#)]
54. Lambe, A.; Ahern, A.; Williams, L.; Slowik, J.; Wong, J.; Abbatt, J.; Brune, W.; Ng, N.; Wright, J.; Croasdale, D.; et al. Characterization of aerosol photooxidation flow reactors: Heterogeneous oxidation, secondary organic aerosol formation and cloud condensation nuclei activity measurements. *Atmos. Meas. Tech.* **2011**, *4*, 445–461. [[CrossRef](#)]
55. Lambe, A.; Chhabra, P.; Onasch, T.; Brune, W.; Hunter, J.; Kroll, J.; Cummings, M.; Brogan, J.; Parmar, Y.; Worsnop, D.; et al. Effect of oxidant concentration, exposure time, and seed particles on secondary organic aerosol chemical composition and yield. *Atmos. Chem. Phys.* **2015**, *15*, 3063–3075. [[CrossRef](#)]
56. Lambe, A.; Ahern, A.; Wright, J.; Croasdale, D.; Davidovits, P.; Onasch, T. Oxidative aging and cloud condensation nuclei activation of laboratory combustion soot. *J. Aerosol Sci.* **2015**, *79*, 31–39. [[CrossRef](#)]
57. Schneider, C.A.; Rasband, W.S.; Eliceiri, K.W. NIH image to ImageJ: 25 years of image analysis. *Nat. Methods* **2012**, *9*, 671–675. [[CrossRef](#)] [[PubMed](#)]

58. Forrest, S.; Witten, T., Jr. Long-range correlations in smoke-particle aggregates. *J. Phys. A Math. Gen.* **1979**, *12*, L109. [[CrossRef](#)]
59. Sorensen, C.; Cai, J.; Lu, N. Light-scattering measurements of monomer size, monomers per aggregate, and fractal dimension for soot aggregates in flames. *Appl. Opt.* **1992**, *31*, 6547–6557. [[CrossRef](#)] [[PubMed](#)]
60. Klein, R.; Meakin, P. Universality in colloid aggregation. *Nature* **1989**, *339*, 360–392.
61. Köylü, Ü.Ö.; Faeth, G.; Farias, T.L.; Carvalho, M.d.G. Fractal and projected structure properties of soot aggregates. *Combust. Flame* **1995**, *100*, 621–633. [[CrossRef](#)]
62. Oh, C.; Sorensen, C. The effect of overlap between monomers on the determination of fractal cluster morphology. *J. Colloid Interface Sci.* **1997**, *193*, 17–25. [[CrossRef](#)] [[PubMed](#)]
63. Raj, A.; Tayouo, R.; Cha, D.; Li, L.; Ismail, M.A.; Chung, S.H. Thermal fragmentation and deactivation of combustion-generated soot particles. *Combust. Flame* **2014**, *161*, 2446–2457. [[CrossRef](#)]
64. Slowik, J.G.; Cross, E.S.; Han, J.-H.; Kolucki, J.; Davidovits, P.; Williams, L.R.; Onasch, T.B.; Jayne, J.T.; Kolb, C.E.; Worsnop, D.R. Measurements of morphology changes of fractal soot particles using coating and denuding experiments: Implications for optical absorption and atmospheric lifetime. *Aerosol Sci. Technol.* **2007**, *41*, 734–750. [[CrossRef](#)]
65. Dhaubhadel, R.; Pierce, F.; Chakrabarti, A.; Sorensen, C. Hybrid superaggregate morphology as a result of aggregation in a cluster-dense aerosol. *Phys. Rev. E* **2006**, *73*, 011404. [[CrossRef](#)] [[PubMed](#)]
66. Slowik, J.G.; Stainken, K.; Davidovits, P.; Williams, L.; Jayne, J.; Kolb, C.; Worsnop, D.R.; Rudich, Y.; DeCarlo, P.F.; Jimenez, J.L. Particle morphology and density characterization by combined mobility and aerodynamic diameter measurements. Part 2: Application to combustion-generated soot aerosols as a function of fuel equivalence ratio. *Aerosol Sci. Technol.* **2004**, *38*, 1206–1222. [[CrossRef](#)]
67. Wilks, D.S. *Statistical Methods in the Atmospheric Sciences*; Academic Press: Cambridge, MA, USA, 2011.
68. Chakrabarty, R.K.; Moosmüller, H.; Arnott, W.P.; Garro, M.A.; Walker, J. Structural and fractal properties of particles emitted from spark ignition engines. *Environ. Sci. Technol.* **2006**, *40*, 6647–6654. [[CrossRef](#)] [[PubMed](#)]
69. Virtanen, A.K.; Ristimäki, J.M.; Vaaraslahti, K.M.; Keskinen, J. Effect of engine load on diesel soot particles. *Environ. Sci. Technol.* **2004**, *38*, 2551–2556. [[CrossRef](#)] [[PubMed](#)]
70. Alfè, M.; Apicella, B.; Barbella, R.; Rouzaud, J.N.; Tregrossi, A.; Ciajolo, A. Structure–property relationship in nanostructures of young and mature soot in premixed flames. *Proc. Combust. Inst.* **2009**, *32*, 697–704. [[CrossRef](#)]
71. Vander Wal, R.L.; Tomasek, A.J. Soot oxidation: Dependence upon initial nanostructure. *Combust. Flame* **2003**, *134*, 1–9. [[CrossRef](#)]
72. Ishiguro, T.; Suzuki, N.; Fujitani, Y.; Morimoto, H. Microstructural changes of diesel soot during oxidation. *Combust. Flame* **1991**, *85*, 1–6. [[CrossRef](#)]
73. Song, J.; Alam, M.; Boehman, A.L.; Kim, U. Examination of the oxidation behavior of biodiesel soot. *Combust. Flame* **2006**, *146*, 589–604. [[CrossRef](#)]
74. Müller, J.-O.; Frank, B.; Jentoft, R.E.; Schlögl, R.; Su, D.S. The oxidation of soot particulate in the presence of NO₂. *Catal. Today* **2012**, *191*, 106–111. [[CrossRef](#)]
75. Kamm, S.; Möhler, O.; Naumann, K.-H.; Saathoff, H.; Schurath, U. The heterogeneous reaction of ozone with soot aerosol. *Atmos. Environ.* **1999**, *33*, 4651–4661. [[CrossRef](#)]
76. Disselkamp, R.; Carpenter, M.; Cowin, J.; Berkowitz, C.; Chapman, E.; Zaveri, R.; Laulainen, N. Ozone loss in soot aerosols. *J. Geophys. Res. Atmos.* **2000**, *105*, 9767–9771. [[CrossRef](#)]
77. Browne, E.C.; Franklin, J.P.; Canagaratna, M.R.; Massoli, P.; Kirchstetter, T.W.; Worsnop, D.R.; Wilson, K.R.; Kroll, J.H. Changes to the chemical composition of soot from heterogeneous oxidation reactions. *J. Phys. Chem. A* **2015**, *119*, 1154–1163. [[CrossRef](#)] [[PubMed](#)]

